Chemistry and Physics of Lipids 220 (2019) 66–76

Contents lists available at ScienceDirect

Chemistry and Physics of Lipids

journal homepage: www.elsevier.com/locate/chemphyslip

Lipid composition and salt concentration as regulatory factors of the anion selectivity of VDAC studied by coarse-grained molecular dynamics simulations

F. Van Liefferinge[a,1], E.-M. Krammer[a,1], D. Sengupta[b], M. Prévost[a,*]

[a] Structure et Fonction des Membranes Biologiques, Université Libre de Bruxelles (ULB), Brussels, Belgium
[b] CSIR-National Chemical Laboratory, Dr. Homi Bhabha Road, Pune, 411 008, India

ARTICLE INFO

Keywords:
VDAC
Membrane channel
Protein-lipid interactions
Coarse-grained molecular dynamics

ABSTRACT

The voltage-dependent anion channel (VDAC) is a mitochondrial outer membrane protein whose fundamental function is to facilitate and regulate the flow of metabolites between the cytosol and the mitochondrial intermembrane space. Using coarse-grained molecular dynamics simulations, we investigated the dependence of VDAC selectivity towards small inorganic anions on two factors: the ionic strength and the lipid composition. In agreement with experimental data we found that VDAC becomes less anion selective with increasing salt concentration due to the screening of a few basic residues that point into the pore lumen. The molecular dynamics simulations provide insight into the regulation mechanism of VDAC selectivity by the composition in the lipid membrane and suggest that the ion distribution is differently modulated by POPE compared to the POPC bilayer. This occurs through the more persistent interactions of acidic residues located at both rims of the β-barrel with head groups of POPE which in turn impact the electrostatic potential and thereby the selectivity of the pore. This mechanism occurs not only in POPE single component membranes but also in a mixed POPE/POPC bilayer by an enrichment of POPE over POPC lipids on the surface of VDAC. Thus we show here that computationally-inexpensive coarse-grained simulations are able to capture, in a semi-quantitative way, essential features of VDAC anion selectivity and could pave the way toward a molecular level understanding of metabolite transport in natural membranes.

1. Introduction

The voltage-dependent anion channel (VDAC) forms the major transport pathway through the mitochondrial outer membrane for small inorganic ions, ATP/ADP exchange as well as for the fluxes of other metabolites and cofactors (Camara et al., 2017; Colombini, 2004; Homblé et al., 2012). At least one VDAC isoform is found in all organisms possessing mitochondria. Upon exposure to voltages higher than about ± 20 mV, the canonical VDAC, reconstituted in planar lipid bilayers, exhibits a transition from an open state to lower conductance states, which are no longer permeable to metabolites (Hodge and Colombini, 1997; Rostovtseva and Colombini, 1997, 1996). This transition has been proposed to occur through a gating process set up by VDAC to control metabolite flux through the mitochondrial outer membrane (Camara et al., 2017; Colombini, 2004; Hodge and Colombini, 1997). The VDAC open state is biochemically and biophysically well characterized. It features a moderate anion selectivity towards small inorganic ions (Colombini, 1989; Hinsch et al., 2004; Homblé et al., 2012) which has been reported to be sensitive to several factors such as the presence of specific residues, the ionic strength and the lipid composition (Krammer et al., 2011; Mlayeh et al., 2017, 2010; Peng et al., 1992; Zambrowicz and Colombini, 1993).

The molecular mechanisms of VDAC functions are unquestionably related to its three dimensional structure and conformational changes. In 2008, three atomic level structures of the mammalian VDAC isoform 1 were reported (Bayrhuber et al., 2008; Hiller et al., 2008; Ujwal et al., 2008) and others followed more recently (Choudhary et al., 2014; Hosaka et al., 2017; Jaremko et al., 2016; Schredelseker et al., 2014). In all these structures, VDAC adopts a unique β-barrel fold composed of 19 β-strands and a N-terminal α-helix leaning onto the inner barrel wall about half way along the pore (Fig. 1). Although these structures have been a matter of some debate (Colombini, 2016, 2009; Hiller et al.,

Abbreviations: BD, Brownian dynamics; CG, coarse-grained; MD, molecular dynamics; VDAC, voltage-dependent anion channel; mVDAC1, mouse VDAC Isoform 1

* Corresponding author.
E-mail address: mprevost@ulb.ac.be (M. Prévost).

[1] These authors contributed equally.

https://doi.org/10.1016/j.chemphyslip.2018.11.002
Received 17 October 2018; Received in revised form 8 November 2018; Accepted 12 November 2018
Available online 15 November 2018
0009-3084/

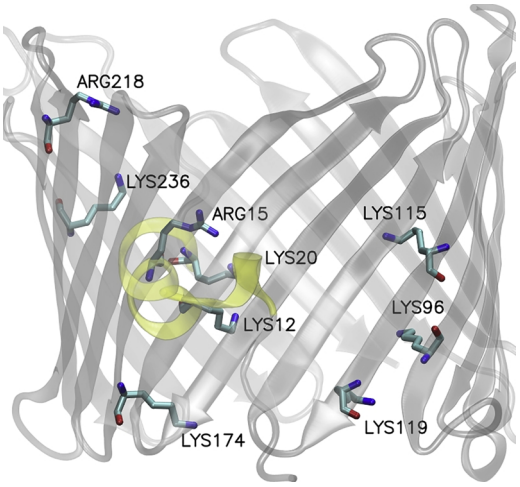

Fig. 1. Side view of the 3D structure of mVDAC1 (PDB ID: 3emn (Ujwal et al., 2008)) shown as a white transparent cartoon. The N-terminal helix is highlighted in yellow. The basic residues found in MD simulations to be important for ion translocation are also depicted as atom-type colored sticks and labeled.

2010) several electrophysiological data obtained in planar lipid bilayers were reported to corroborate the VDAC structures representing its open state (Choudhary et al., 2014; Hiller et al., 2010; Krammer et al., 2015, 2014, 2011; Lee et al., 2011; Noskov et al., 2013; Rui et al., 2011; Teijido et al., 2014; Villinger et al., 2010; Weiser et al., 2014; Zachariae et al., 2012).

The determination of VDAC open state structures have paved the way for unraveling the basic principles of the channel functions and regulations using theoretical studies as they represent a powerful approach for understanding a variety of biological molecular processes. In particular, all atom (atomistic) molecular dynamics (MD) and Brownian dynamics (BD) simulations have been used to investigate the mechanism of small inorganic ion and metabolite translocation through VDAC (Fig. 1) (Choudhary et al., 2010; Krammer et al., 2015, 2014, 2013, 2011; Lee et al., 2011; Mlayeh et al., 2017; Rui et al., 2011). They showed that VDAC selectivity towards small inorganic anions is promoted by the distribution of charged residues inside the pore creating, at low salt concentration, a favorable electrostatic potential and that it diminishes with increasing concentration due to a screening of the protein charges (Krammer et al., 2014, 2013). Likewise atomistic MD simulations proposed a mechanism rationalizing the regulation of plant VDAC selectivity occurring upon a change of choline into ethanolamine phospholipid head group which would arise from specific interactions made by acidic residues only with the ethanolamine group (Mlayeh et al., 2017).

Despite the steady increase in computational power, applications of atomistic MD which provide a detailed insight into the role of specific interactions in biological systems are still limited to relatively small systems and/or to rather fast processes. In contrast simulations of coarse-grained (CG) protein models which assume different levels of reduced representation of proteins and of their molecular surroundings, e.g. lipids, water, ions (Baaden and Marrink, 2013; Ingólfsson et al., 2014; Morriss-Andrews and Shea, 2014) offer advantages over the atomistic ones as they enable simulations of longer time-scales and/or larger molecular systems (Stansfeld and Sansom, 2011). However, there are important limitations to the CG models as well. The major drawback is the neglection of the atomistic degrees of freedom. For instance, the CG Martini force field, in which the parameterization is based on free energies, may lead to modified enthalpies due to the inherent entropy loss on coarse graining (Periole and Marrink, 2013). An increasing number of CG MD studies on membrane proteins has been published (Bradley and Radhakrishnan, 2013; Dreyer et al., 2013; Hung and Yarovsky, 2011; Ingólfsson et al., 2014; Kmiecik et al., 2016; Vorobyov et al., 2016; Yefimov et al., 2008) and CG models, in particular the MARTINI one, were fairly successful in identifying lipid binding sites, in particular, in α-helical membrane proteins (Arnarez et al., 2013; Sengupta and Chattopadhyay, 2012; Stansfeld et al., 2009; Yin and Kindt, 2012). In that respect β-barrel membrane proteins have been more sparsely studied (Dreyer et al., 2013; Yin and Kindt, 2012).

In this study we examined the capacity of CG MD simulations to describe the permeation of small inorganic ions through the β-barrel shaped pore mouse VDAC1 (mVDAC1). The role of two particular factors affecting VDAC selectivity are particularly addressed: one is the salt concentration and the other is the nature of the membrane phospholipid headgroup.

2. Material and methods

2.1. Brownian dynamics simulations

All BD inputs were created with the GCMC/BD module (Lee et al., 2012) of the CHARMM GUI server (Jo et al., 2008) using the mVDAC1 crystal structure (Ujwal et al., 2008). All BD simulations were performed using the GCMC/BD program (Im et al., 2000). The parameters were taken as described elsewhere (Krammer et al., 2014). To describe the diffusion profile of the ions inside the pore a position-dependent scaling of the diffusion coefficient was applied (Lee et al., 2012; Paine and Scherr, 1975). All simulation time lengths are summarized in Table 1.

2.2. All-atom molecular dynamics simulations

The mVDAC1 protein (PDB ID: 3EMN) was inserted in a lipid bilayer

Table 1
Overview of the performed simulations. For each simulation type (BD, atomistic and CG MD) the simulation length of each trajectory and the number of trajectories per system (in brackets) are given. Atomistic (AA) and CG MD simulations were performed in either POPC or POPE except a CG MD which was carried out in an equal mixture of POPC and POPE lipids.

	0.05 M	0.1 M	0.15 M	0.2 M	0.4 M	0.6 M	0.8 M	1.0 M
BD	2 μs (10)	1 μs (10)	500 ns (10)	500 ns (10)	250 ns (10)	200 ns (10)	100 ns (10)	100 ns (10)
AA (POPC)	/	100 ns (5)	100 ns (5)	75 ns (5)	75 ns (3)	50 ns (2)	50 ns (2)	50 ns (2)
AA (POPE)	/	100 ns (5)	100 ns (5)	75 ns (5)	75 ns (3)	50 ns (2)	50 ns (2)	50 ns (2)
CG (POPC)	1 μs (5)	1 μs (5)	1 μs (5)	1 μs (5)	1 μs (5)	1 μs (5)	1 μs (5)	1 μs (5)
CG (POPE)	1 μs (5)	1 μs (5)	1 μs (5)	1 μs (5)	1 μs (5)	1 μs (5)	1 μs (5)	1 μs (5)
CG mix (POPC/POPE)	/	/	/	10 μs (5)	/	/	/	/

using the CHARMM-GUI web server as previously described (Krammer et al., 2011). The atomistic MD trajectories were generated with the program NAMD2.9 (Phillips et al., 2005). The CHARMM36 force field (Best et al., 2012) with CMAP corrections (MacKerell et al., 1998) was used for protein, ions, and water. The lipid molecules were described by a united atom force field (Lee et al., 2014). All other parameter settings were defined as described elsewhere (Krammer et al., 2011). A time step of 2 fs was used for the simulations with neighbor list updated every 2 steps. Depending on the salt concentration value, two to five independent trajectories of mVDAC1 embedded either in POPE or POPC bilayers were performed and the time span of the simulations ranged between 100–500 ns (Table 1). The POPE/POPC containing systems comprised 180/155 lipids and about 8900/9100 water molecules.

2.3. Coarse-grained molecular dynamics simulations

All CG MD simulations were carried out using GROMACS4.5.5 (Van Der Spoel et al., 2005), with the MARTINI2.2 force field (Marrink et al., 2007; Monticelli et al., 2008) and the polarizable water model (Yesylevskyy et al., 2010). Energy minimization was carried out using steepest descent algorithm. A shift potential was applied to non-bonded interactions with the standard cut-offs in the MARTINI force-field. Temperature of each molecular group in the system was weakly coupled to a thermostat at 300 K using the v-rescale algorithm (Bussi et al., 2007) with a coupling constant of 1 ps. Semi-isotropic pressure coupling was maintained at 1 bar independently in the plane of the bilayer and perpendicular to the bilayer using Parrinello-Rahman's barostat algorithm (Parrinello and Rahman, 1981) with a coupling constant of 12 ps and a compressibility of 3×10^{-4} bar^{-1}. Initial velocities for the simulations were chosen randomly from a Maxwell distribution at 300 K. Bond lengths were kept constant using the LINCS algorithm (Hess et al., 1997). A time step of 20 fs was used for the simulations with neighbor list updated every 10 steps. Periodic boundary conditions were maintained along x, y and z direction. Each system comprises 266 lipids and about 6700 water sites. Five independent trajectories of 1μs, 1 μs and 10 μs were performed with mVDAC1 embedded either in POPE or POPC or in equal mixture of POPE/POPC bilayers (Table 1). The last 2 μs were analyzed in the case of the POPE/POPC mixture trajectories.

2.4. Analysis of the trajectories

For all simulations the ratio of the time-averaged number of chloride (N_{Cl}^-) and potassium (N_K^+) ions inside the pore was calculated. VDAC pore location was defined from −15 to 15 Å along the z axis in the BD simulations. In both atomistic and CG MD simulations the pore was defined as a cylinder with a radius of 17 Å, and a length ranging from −15 to 15 Å along its inertia main axis aligned with the z axis normal to the membrane and after centering of the protein.

The time-averaged multi-ion free energy profile along the pore axis at 0.1 M and 1.0 M KCl was computed using all atomistic and CG MD simulations for each of the two ionic concentrations. The free energy of an ion species *i* inside the channel at a position z was calculated using the following equation (Marrink and Berendsen, 1994):

$$\Delta G_i(z) = -RTln\frac{C_i(z)}{C_{bulk}}$$

where R, T, $C_i(z)$ and C_{bulk} are the gas constant, the temperature, the concentration inside the pore at z, and bulk concentration of the ionic species *i*, respectively. $C_i(z)$ was determined by dividing the simulation box into 1 Å wide slices. This method has been successfully used for the determination of the free energy profile of small compounds inside protein pores (Luo et al., 2010; Wang et al., 2007) and also of ions inside human VDAC1 (Rui et al., 2011) and mVDAC1 (Krammer et al., 2015, 2013, 2011).

Different interactions were monitored in the atomistic and CG MD trajectories. An interaction between Cl^-/K^+ ions and oxygen atom of acidic or nitrogen of basic residue sidechains was counted for a distance less than 4 (atomistic MD) and 6 (CG MD) Å, respectively. Likewise, an interaction between acidic residue and lipid head groups was defined to occur for a distance between the nitrogen of the lipid and the side chain oxygen atom of acidic residue less than 5 (atomistic MD) and 7 (CG MD) Å, respectively. The use of different distances for atomistic and CG MD analyses account for the different van der Waals radii values in the two force fields.

The electrostatic potential maps were obtained using the PMEpot module of vmd with the default values (Aksimentiev and Schulten, 2005).

The maximum occupancy time was defined as the longest time a given POPE or POPC head group was bound at a particular site and calculated with the g_mindist module from GROMACS. The values were normalized for all simulation lengths. A value of one implies that the same head group was present at the site during the entire simulation, and zero implies that it was never present at that site.

The spatial density of POPE and POPC was calculated over the full trajectories using g spatial from GROMACS. For infinitely long sampling, the total occupancy corresponds to the average spatial density.

3. Results

3.1. Concentration dependence of VDAC selectivity

In the first step, we explored the permeation of inorganic ions through mVDAC1 using CG MD simulations, and evaluated its selectivity as a function of the KCl concentration. As a measure of the ion selectivity, we considered the N_{Cl}^-/N_K^+ ratio, where N_{Cl}^- and N_K^+ are the time-averaged number of chloride and potassium ions respectively inside the pore, computed over the trajectories. The N_{Cl}^-/N_K^+ ratio inside the channel is higher at low salt concentration and decreases non-linearly with increasing salt concentration in the CG simulations (Fig. 2). This non linear decrease is in line with experimental data (Krammer et al., 2014; Zambrowicz and Colombini, 1993). For comparison, we also calculated the N_{Cl}^-/N_K^+ ratio from atomistic and BD MD simulations. The dependence of this ratio with the salt concentration is quite similar in both BD and atomistic MDs, and more pronounced compared to that of CG simulations (Fig. 2).

In the next step, we analyzed in detail the distribution of potassium and chloride ions during the permeation events at the two extreme KCl concentrations, 0.1 M and 1.0 M KCl. In the CG MD simulations at 0.1 M concentration, no long-lived interactions are formed between protein residues and chloride ions in the channel (Fig. S1A). Chloride ions interact with basic residues in about 1.5–35 % of the MD trajectories with the highest percentages observed for two arginine residues, R15 (34.2%) and R218 (20.6%) (Table 2A). The positively charged residues that contribute to enhance the density of chloride ions in their vicinity all point into the lumen of VDAC. In contrast, potassium ions formed interactions with very few acidic residues, in less than 1.5% of the trajectories (Table 2B) except for one ionic interaction formed with D186 (~10%). In contrast to the basic residues favoring the presence of chloride ions the acidic residues interacting with potassium ions are located at the rim of the channel.

Interestingly, although the trends are similar in the atomistic trajectories, the main interactions of the chloride ions are formed not with arginine but with two lysine residues, K12 (14.2%) and K20 (12.8%) (Table 2A, Fig. S1B). Potassium ions were observed to interact with very few acidic residues and with low percentages (≤1.5%) (Table 2B, Fig. S1D). The main exception was the ionic interaction formed with D264 located in an external loop that “traps” a potassium ion during the simulations.

The overlap of ion positions along the trajectories provides a qualitative information on the average distribution of ions. In the CG simulations performed at 0.1 M, the superimposition of the ion configurations reveals a few regions of higher chloride density (Fig. 3). The

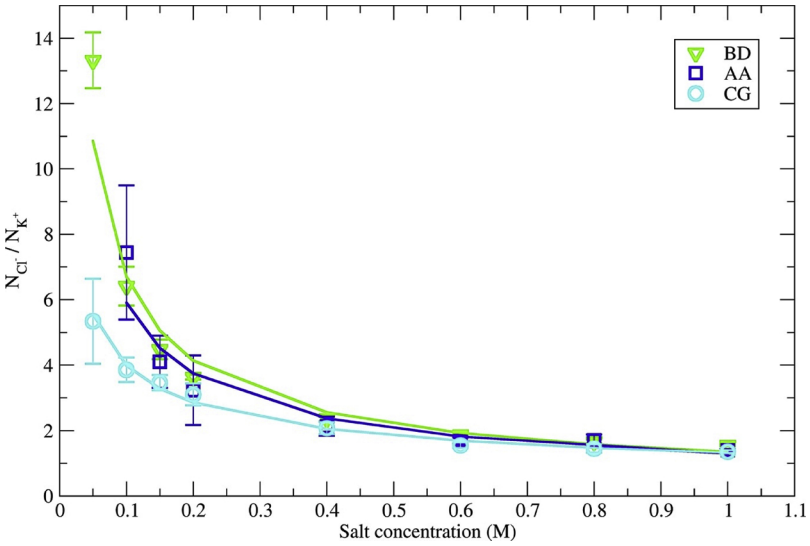

Fig. 2. Selectivity of mVDAC1. N_{Cl^-}/N_{K^+} ratio as a function of the KCl bulk concentration computed with CG MD (cyan circle), atomistic MD (AA) (blue square) and BD (green triangle) trajectories. For each data point the standard error is shown as a bar. A nonlinear least square regression using a power fitting function of the type $y = ax^b$ (a and b values are given in Table S1) was used to fit the data points (solid lines). Only the CG MD and BD simulations were performed at the very low 0.05 M KCl concentration as atomistic MD lacked statistics at that concentration.

first site is located at the level of the helix, supported by interactions of chloride ions with the helical residues, K12, R15 and K20 (see Fig. 1 for localization of basic residues mentioned in the text). A second occurs on the cytosolic side of the helix sandwiched between the helical residue R15 and the cytosolic side residues R218 and K236. Another cluster, roughly localized between the intermembrane space side and the helix, is promoted by K96, K115 and K119 from adjacent β-strands as well as K174. These clusters are also observed in atomistic MD trajectories except that the magnitude of their densities differs compared to that from CG MDs (Fig. 3). The pore lumen shows no particular cluster of potassium ions.

At 1 M KCl the number of ions in the vicinity of charged residues increases compared to the situation at 0.1 M in both CG and atomistic trajectories. The percentage of the interactions between the ions and charged residues is overall significantly higher illustrating the screening of the charged residue upon increasing salt concentration (Table 2C, D and Fig. S2).

The multi-ion free energy profiles of chloride and potassium permeation were computed along the VDAC pore axis from the CG MD and atomistic MD trajectories at 0.1 M and 1 M KCl (Fig. 4). At 0.1 M salt concentration, in CG as well as in the atomistic simulations, the Cl^- ions cross on either side of the pore, a quasi-symmetric barrier. These two barriers arise from the presence of the lipid bilayer as both CG and atomistic profiles computed in a system enclosing VDAC along with bulk water and ions and excluding most lipids lack these peaks (Fig. S3). Entering the pore from the intermembrane space side, chloride ions encounter two shallow wells which comprise a region containing part of the N-terminal helix (Fig. S4). These two minima merge into one slightly deeper minimum in atomistic MDs. Further in the pore, another deep well occurs between the helix and the cytosolic side (Fig. S4) in both the CG and atomistic profiles albeit shallower in the latter. As for potassium, a single barrier arises inside the pore, in the CG profile, at the level of the N-terminal helix on the intermembrane side, whereas two occur in the atomistic MDs that correspond to the two chloride wells found on the intermembrane and cytosolic sides. Overall, the CG and atomistic simulation chloride and potassium profiles in VDAC pore indicates a preference for chloride versus potassium. However, the energy difference between K^+ and Cl^- profiles at the location of the energy wells is smaller for CG MD compared to atomistic MD. This is in line with a lower selectivity found in the CG simulations compared to that in the atomistic MDs (Fig. 2). At the higher salt concentration (1.0 M), the energy wells of chloride are flattened and, the energy barriers of potassium are significantly reduced relative to 0.1 M in both CG and atomistic MDs (Fig. 4B).

The time-averaged electrostatic potential calculated from the CG and atomistic trajectories at 0.1 M KCl reveals a positive potential in the pore that accounts for the anionic selectivity of VDAC (Fig. 5). This is consistent with mutagenesis experiments which showed the importance of several basic residues, located in the lumen, for the selectivity of yeast VDAC (Blachly-Dyson et al., 1990). In the electrostatic map obtained from the atomistic MD (Fig. 5), the interior of the lipid appears positively biased by about 1 V relative to the bulk of the solution in agreement with experimentally measured dipole potentials (Wang, 2012). This is not the case for the potential calculated from the CG MD trajectories which is negative and has been attributed to the water model which cannot fully compensate for the lipid potential (Yesylevskyy et al., 2010). Nevertheless, in both CG and atomistic maps, the channel confines most of the positive electrostatic potential that drives the chloride ions. Furthermore, the strongest positive potential zones in the channel match the different highest densities of chloride (Fig. 3).

3.2. Lipid head group affects VDAC selectivity

To contrast the selectivity of the POPE head group, we investigated the permeation of ions through mVDAC1 embedded in a POPC bilayer. In POPC, the VDAC selectivity decreases with the salt concentration in both CG and atomistic MD (Fig. 6A) similar to that in POPE (Fig. 2). At low salt concentrations, however, VDAC selectivity is less anionic in POPC than in POPE irrespective of the resolution of the force-field, in agreement with data recently reported on plant VDAC (Mlayeh et al., 2017). Upon increasing salt concentrations, the selectivity in POPC and POPE converges to a similar value.

A detailed comparison of N_{K^+} and N_{Cl^-}, the individual ion numbers inside the pore, averaged over the CG trajectories is shown in Table S2. It can be seen that the higher anion selectivity, at low salt concentration, in POPE compared to POPC membranes, arises mainly from a decrease in the number of potassium ions together with a slight increase in the number of chloride ions inside the pore (Table S2). A similar trend is observed in the atomistic MD simulations. Thus to decipher the molecular basis for this selectivity change the interactions formed between the ions and VDAC residues were monitored. As seen in POPE bilayer no long-lived interactions are observed in POPC bilayer (Fig. S5). At low salt concentration, the percentage of interactions formed by chloride ions with basic residues is slightly higher in POPE versus POPC lipid membrane environment whereas the reverse trend is observed for interactions of potassium with acidic residues (Table 2A, B). The trends are more pronounced in the atomistic simulations (Table 2A, B).

Table 2
Interactions between chloride or potassium ions and protein residues of VDAC. Percentage of interactions formed by chloride ions with basic residue side chains (A, C) and by potassium ions with acidic residue sidechains (B, D) at 0.1 M KCl (A, B) extracted from 5-μs long CG or 500-ns long atomistic (AA) MD simulations and at 1 M KCl (C, D) extracted from 2.5 μs CG and 500 ns atomistic MD simulations, of mVDAC1 embedded in a POPE or POPC membrane. Only residues with a percentage higher than 5% (0.1 M) or 20% (1 M) in at least one type of simulations are listed.

A

	Chloride			
0.1 M	POPE		POPC	
Residue #	CG	AA	CG	AA
K12	4.8	14.2	3.5	13.8
R15	34.2	8.9	34.5	5.2
K20	4.9	12.8	4.1	11.9
K32	1.5	5.4	0.8	3.6
K96	2.2	8.2	1.7	6.4
K115	1.4	6.9	0.4	1.4
K119	1.6	7.8	1.5	8
K174	1.4	7.5	1.1	8.1
R218	20.6	8.5	22.5	6.2
K236	11.2	12.2	9.7	11.6

B

	Potassium			
0.1 M	POPE		POPC	
Residue #	CG	AA	CG	AA
E177	1.3	1	1.5	5.4
D186	10	1.5	13.3	4
D228	1.4	0.5	1.6	7.7
D264*	0.1	33.5	0.1	6

C

	Chloride			
1 M	POPE		POPC	
Residue #	CG	AA	CG	AA
K12	24.6	40.5	22	49.5
R15	78.8	28	82.5	21.9
K20	34	37.2	30.9	44.8
K32	7.5	11	11.1	22.9
K34	12.3	18.4	7	20.9
K53	27.9	19.6	27.4	19.5
R63	21.9	11.7	20.1	12.4
R93	5.2	23.7	5.9	29.7
K96	7.7	12.4	16.8	42.8
K109	43.8	21.5	37.9	14.3
K113	8.2	22	7.8	14.2
K115	9.4	22.4	15.5	21.4
K119	8.4	25.6	9.1	46.4
R139	20.1	20.9	19.2	35.4
K161	21.9	17.5	20.4	25.5
K174	9.4	27.5	8.1	35.8
K200	22.3	35.5	23.3	28.3
R218	61.2	27.6	65.1	25
K236	35.6	44.4	51.9	26.1
K256	22.3	19.3	24.9	19.6

D

	Potassium			
1 M	POPE		POPC	
Residue #	CG	AA	CG	AA
E36	19.8	20.7	19.2	27.3
E50	26.2	15.9	26.5	14.1
E59	12	16.3	12.8	28

(*continued on next page*)

Table 2 (*continued*)

D

	Potassium			
1 M	POPE		POPC	
Residue #	CG	AA	CG	AA
E66	46.5	18.2	46.2	20.3
D78	27.8	16.1	30.5	18.1
E88	30.9	14.9	28.2	15.6
D100	7.4	22.7	8.8	37.5
D132	21.7	14.1	23.7	20.3
E147	29.1	15.1	33.2	18.9
E158	20.4	19.3	22.1	21
D176	22.8	21.8	16.3	18.7
E177	20.4	5.7	20.3	36.5
D186	59.5	16.6	58.4	14.4
E189	41.5	23	41.8	23.9
E203	22.4	8.9	15.7	6
D228	14.6	4.9	21.1	26.1
D230	16.6	12.3	25.2	24.2
D264*	1.41	88.5	1.4	49.6
E73[&]	94.6	0	91	0

*The high percentage of interactions results from one potassium ion being trapped in an external loop containing D264 (B, D). [&] Potassium ions penetrate the membrane along VDAC pore to interact with E73 (D) located in β-strand 4 which points to the hydrophobic part of the membrane in all determined 3D structures.

Since POPE and POPC have identical acyl chains, the difference in the VDAC selectivity is likely to arise from the different nature of the substituents on their headgroup nitrogen. The POPE polar head group contains a primary amine (-NH_3) while in POPC the nitrogen atom has three methyl substituents (-$N(CH_3)_3$). We thus monitored the interactions formed between the polar head of lipids and the side chain of acidic residues in both lipid environment simulations. Remarkably, in both CG and atomistic simulations, the POPE polar head forms a significantly higher percentage of interactions with acidic residue side chains reaching a highest 35% (CG) or 46% (atomistic) compared to that of POPC which forms less frequent interactions with a maximum percentage of about 27% (CG) or 26% (atomistic) (Fig. 6B, C). To interact preferably with the POPE polar head these acidic residues which are located at the rim of VDAC pore (Fig. 7C) have their side chains oriented opposite the pore lumen. This should affect to a certain extent the electrostatic potential at the mouth of the channel as shown indeed by a more positive electrostatic potential (Fig. 5) which in turn should favor the entrance of chloride ions promoting a higher anion selectivity of VDAC. In contrast the fewer specific interactions between POPC and the acidic side chains promotes a weaker positive electrostatic potential at the mouth of the VDAC pore (Fig. 5) favoring the entrance of a higher number of potassium ions and thus lowering the selectivity. The difference in selectivity between POPE and POPC fades with increasing salt concentration. This does not result from a global screening of the POPE-acidic residue interactions as they are not affected by KCl concentration (Fig. 6B, C) although some individual interactions are observed to be either enhanced or weakened when going from 0.1 to 1 M (Fig. 7A, B). These same acidic residues are however screened by a high K^+ concentration (Table 2) but this effect does not induce a decrease in their interactions with POPE (Fig. S6). Thus fairly strong ionic

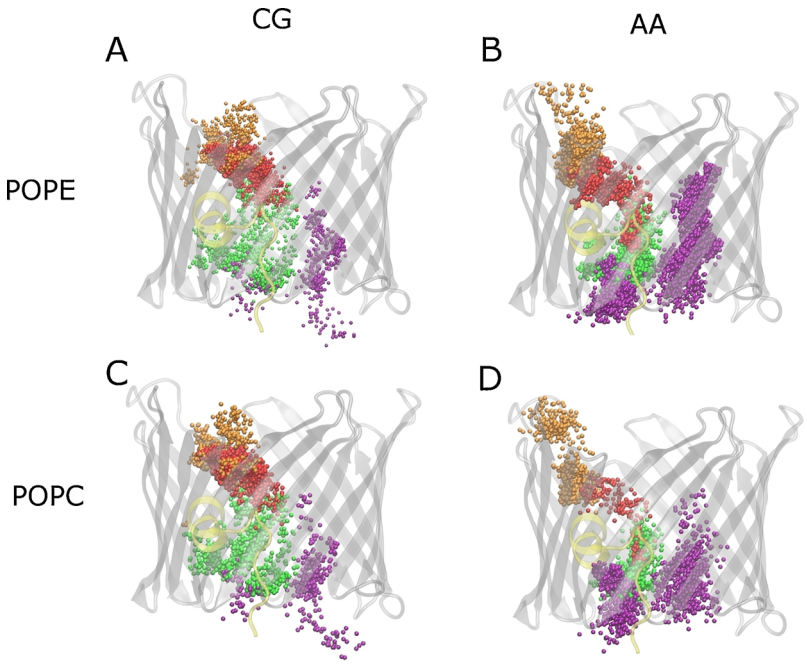

Fig. 3. Distribution of Cl^- in CG and atomistic (AA) MD trajectories. Positions of the Cl^- ions within 6 (in CG) and 4 (in atomistic) Å of the protein residues are superimposed using snapshots extracted every 500 ps from the 0.1 M KCl trajectories in CG (A, C) and atomistic (B, D) trajectories with POPE (A, B) or POPC (C, D). Ions located in the neighborhood of R218, K236 or K12, K20 or K96, K115, K119, K174 are colored in orange, green, and purple, respectively. Those colored in red are in the vicinity of R15 which, depending on its side chain orientation, belongs to the N-terminal helix cluster formed by K12 and K20 or to the cytosolic side group formed by R218 and K236. The position of these residues is shown in Fig. 1. The protein is shown as a white transparent cartoon and the N-terminal helix is colored in transparent yellow.

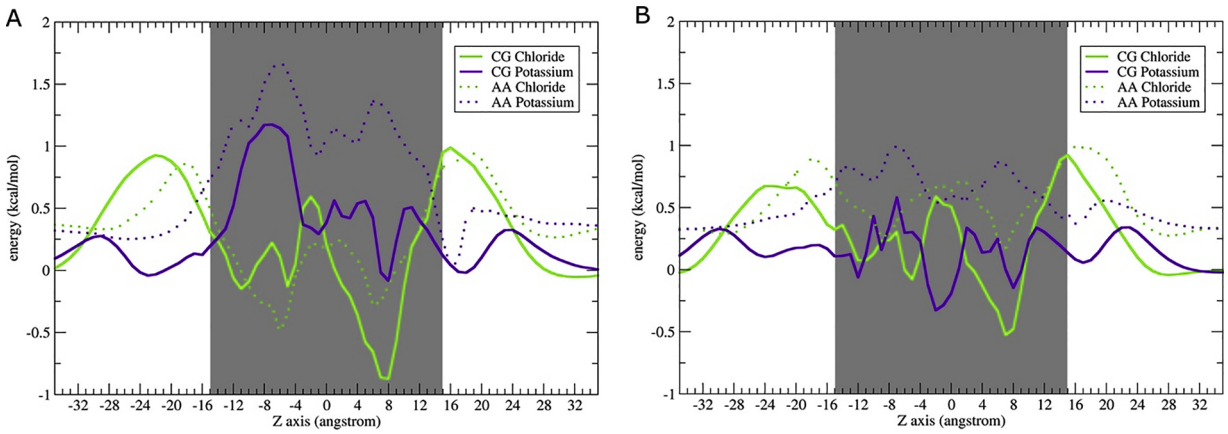

Fig. 4. The ion translocation profile through the pore is concentration dependent. The free energy profiles were computed at (A) 0.1 M and (B) 1.0 M KCl using the CG MD (solid lines) and the atomistic (AA) MD (dotted line) trajectories. Permeation profiles were determined along the axis of the pore for K^+ (purple) and Cl^- (green) in 5 μs CG and 500 ns atomistic trajectories using snapshots every 10 and 2 ps, respectively. The region inside the pore is highlighted by a grey background.

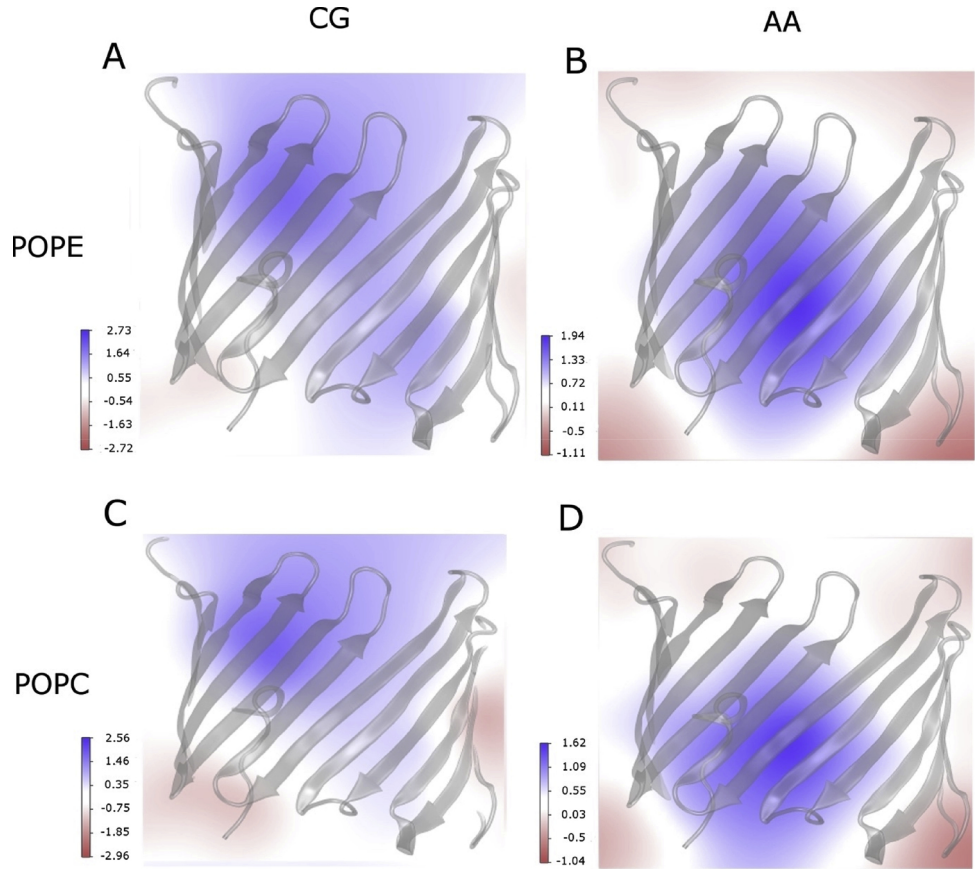

Fig. 5. Cross sectional view of electrostatic potential maps of VDAC along the x axis averaged over the whole CG MD in POPE (A), atomistic (AA) MD in POPE (B), CG MD in POPC (C) and atomistic (AA) MD in POPC (D). Color coding of the electrostatic potential values in volts is also shown.

interactions of acidic residues located at the rim of VDAC pore which occurs with the head group of POPE head group and not POPC enhances the anionic selectivity of the channel.

To examine further the role of phospholipid head groups on VDAC selectivity we performed simulations of VDAC embedded in a bilayer formed with an equal mixture of POPE and POPC in a 0.2 M salt concentration. As lateral diffusion of lipids is one of the major impediments in simulations of lipid mixtures we only used the CG model for increased sampling (Marrink et al., 2007). To get insight into the distribution of POPE/POPC, we analyzed the density of their polar head around the VDAC barrel. In the course of these simulations the surface of VDAC gets markedly enriched in POPE head groups compared to POPC in particular on the intermembrane side (Fig. 8A and S7). To identify the VDAC sites close to the local high lipid densities we then examined the maximum occupancy of each type of lipid head group around the acidic sidechains. We found that about 70% of the acidic residues feature an increase up to 20% of their interactions with POPE relative to POPC (Fig. 8B). For the sake of comparison, we also computed the maximum occupancy in the pure POPE and POPC bilayer CG simulations. Likewise, the acidic residues located at the rims of VDAC pore feature a maximum occupancy of POPE significantly higher than that of POPC (Fig. 8C) as in the POPE/POPC mixture CG simulations.

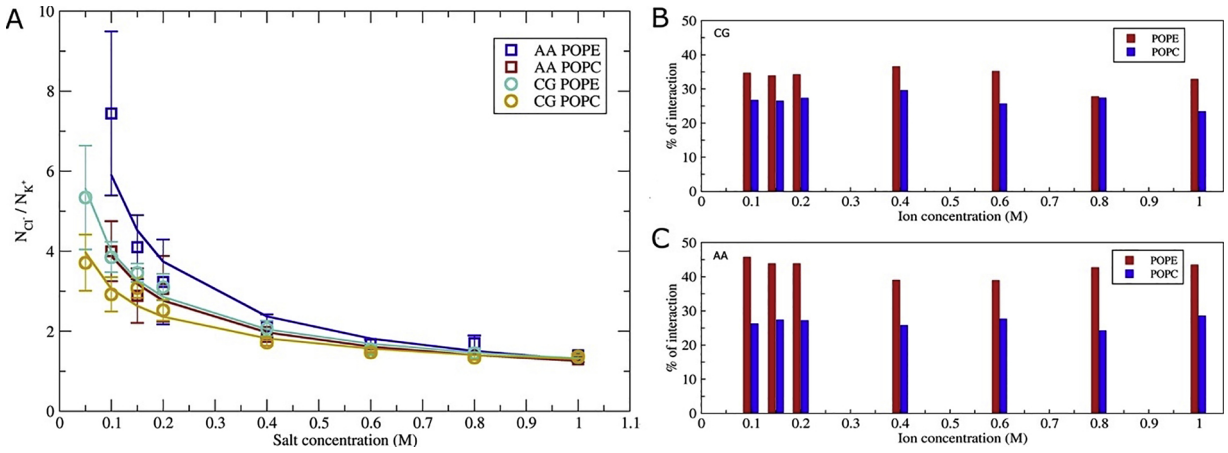

Fig. 6. The VDAC selectivity is affected by the nature of the lipid. (A) The selectivity measured as the N_{Cl}^-/N_K^+ ratio as a function of the bulk KCl concentration for VDAC embedded in either POPE or POPC bilayer (CG MD/POPE (cyan spheres), CG MD/POPC **(orange** spheres), atomistic MD/POPE (blue square), atomistic MD/POPC (red square)). For each data point the standard error is shown as a bar. The fitting procedure is described in Fig. 2. (B, C) Percentage of interactions formed between the lipid head amine group of POPE (red bar) or POPC (blue bar) and the side chain of all VDAC acidic residues as a function of salt concentration in CG (B) and atomistic (AA) (C) MD simulations.

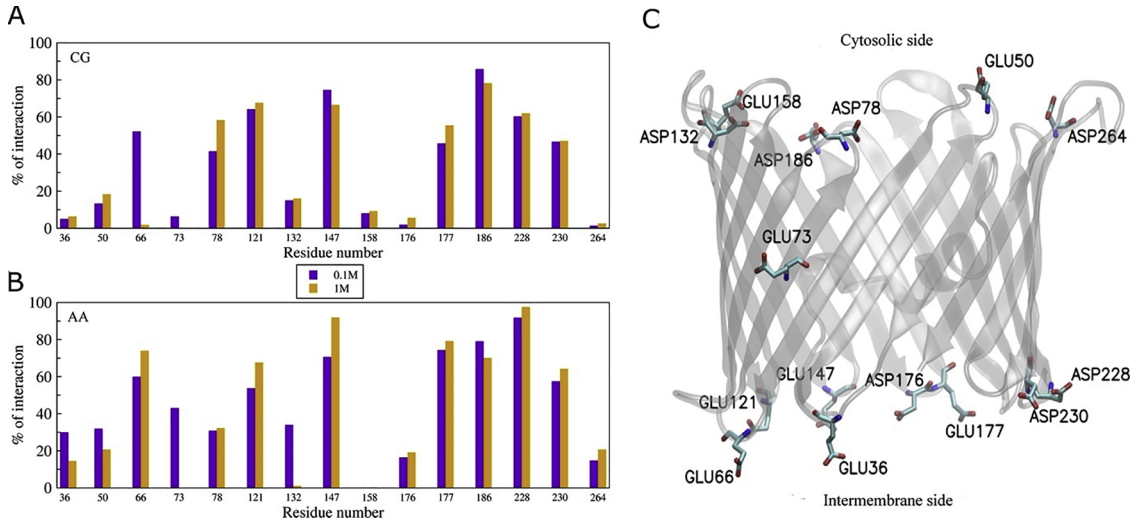

Fig. 7. Percentage of interactions formed between the lipid head amine group of POPE and side chain of VDAC individual acidic residues at 0.1 (purple bar) and 1 M (orange bar) KCl in CG (A) and atomistic (AA) (B) MD simulations. C. Locations of acidic residues forming interactions with the POPE amine group featuring a percentage higher than about 10% in CG MD and atomistic MD. The only acidic residue which is not located at the rim of the channel but nevertheless interacts with POPE head group is E73. This residue is located in the middle of β-strand 4 and points towards the hydrophobic membrane environment in all determined 3D structures (C). The binding of dicyclohexylcarbodiimide, a chemical that covalently links acidic residues in a hydrophobic environment, to E73 supports this unusual surrounding for an acidic residue (De Pinto et al., 1993).

4. Discussion

The molecular mechanisms through which VDAC regulates its selectivity remain to be understood in detail. Here we show that CG simulations performed with the MARTINI force field are able to capture key features of two factors regulating ion selectivity, the salt concentration and the lipid composition, with the outlook towards metabolite transport. Our results indicate that, at low salt concentration, the distribution of basic residues in the lumen controls VDAC anionic selectivity. Specific interactions of POPE lipids with acidic residues of VDAC further modulate this selectivity.

Our simulations show that, in keeping with experimental data (Krammer et al., 2014), the computed selectivity towards anions fades as salt concentration increases. At low salt concentrations, the permeation of chloride ions is facilitated, by an overall electrostatic potential created by the distribution of the charged residues in VDAC pore and is hindered at high salt concentrations due to a screening of these charged residues. The free energy surface profile for chloride and potassium translocation through VDAC at 0.1 M provides further evidence for the protein electrostatics as the main determinant of the pore selectivity. The CG simulations point to two main pore regions which are favorably sampled by the chloride ions. One is located between the N-terminal helix and the extracellular medium and contains Arg15 and Arg218 side chains which have been reported, in several studies to be key partners of ATP during its permeation through VDAC1 (Choudhary et al., 2014; Krammer et al., 2015; Noskov et al., 2013). The other region encompasses the part of the N-terminal helix oriented towards the intermembrane space which contains K12 and K20. These two lysine residues were reported to be involved in the binding of ATP (Choudhary et al., 2014; Krammer et al., 2015; Noskov et al., 2013; Villinger et al., 2014) and substitution, in *S. cerevisiae* VDAC, of the conserved K20 into glutamate was found to induce a change in ion preference (Blachly-Dyson et al., 1990). In contrast a fairly high energy barrier, matching the shallowest chloride wells, prevents potassium from crossing the pore. The quasi absence of potassium barrier in the pore region featuring a deep chloride well can be rationalized by a favorable positive

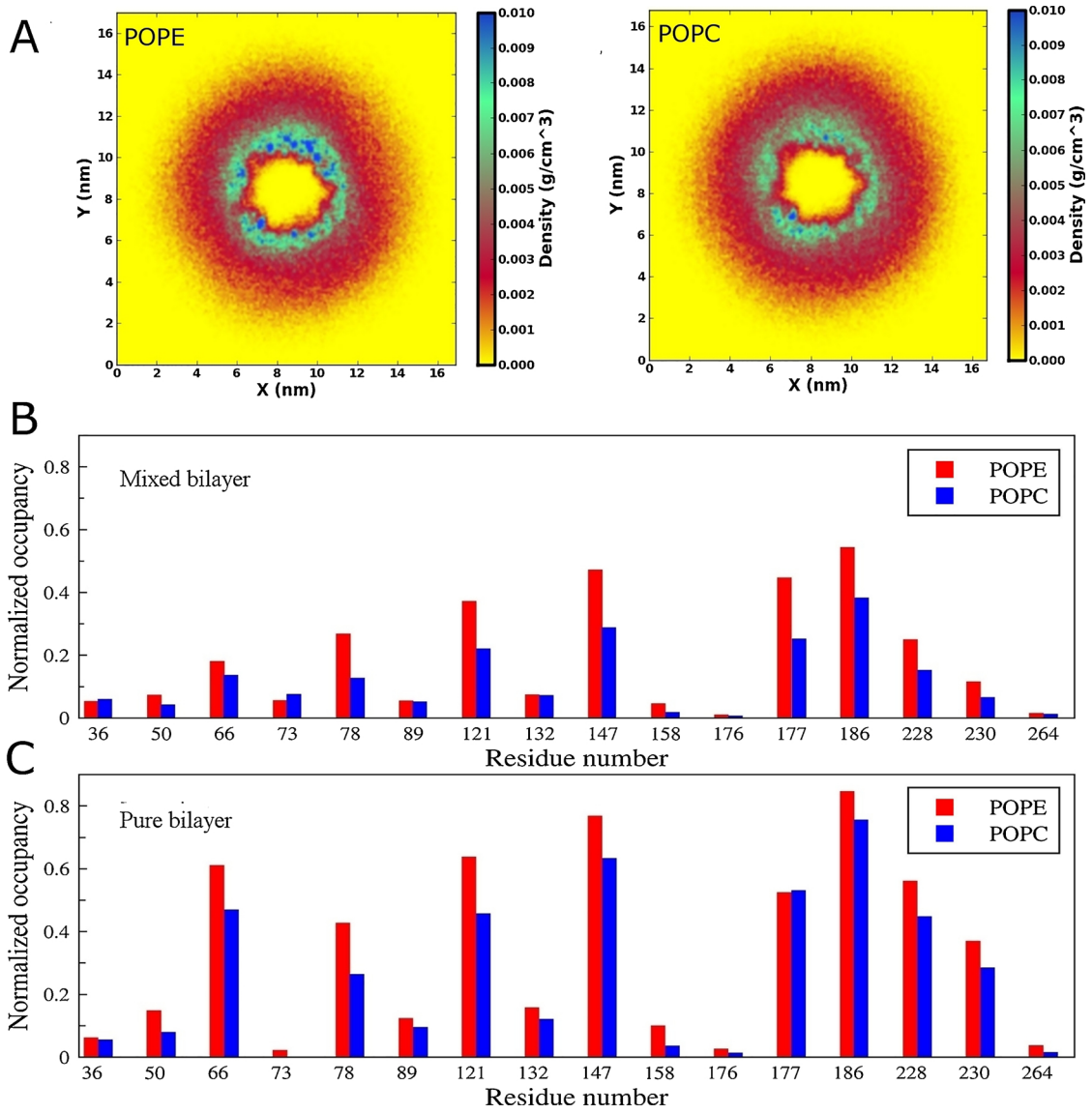

Fig. 8. Interaction of VDAC acidic residues with lipid molecules. (A) 2-D projections of the spatial density function (SDF) of POPE and POPC amine head group around the intermembrane opening region of VDAC. The SDFs were calculated for a Z-slice 10 Å wide containing the intermembrane space head group region in the POPE/POPC mixture CG simulations. A density color scale is shown on the right. (B–C) Normalized maximum occupancy calculated around each VDAC acidic residue side chain, averaged over CG simulations in (B) POPC/POPE mixed bilayer and (C) pure POPE and pure POPC bilayers.

electrostatic potential created by a high density of chloride ions which in turn favors the dwelling of potassium ions.

Although the distribution of ions in the pore lumen is similar in both CG and atomistic simulations, the interactions between chloride ions and arginine residues occur with a significantly higher percentage in CG than in atomistic MD trajectories whereas the reverse is observed for lysine. These differences might be rationalized by the description of these two residue side chains in the MARTINI2.2 (Monticelli et al., 2008) and the CHARMM36 force field (Best et al., 2012). In the CG force field, the Lennard-Jones potential modelling the interaction of chloride ions with the arginine aliphatic moiety is more attractive than for lysine. In contrast in the atomistic force field the main difference in these interaction potentials occurs via the charge distribution which in lysine is localized on its small NH_3 group whereas that of arginine is scattered over the bulkier guanidinium group. These differences can also provide a rationale for the lower selectivity observed in CG compared to atomistic MDs at low salt concentration as VDAC pore is lined by a significant higher number of lysine compared to arginine residues (Table 2A; Fig. 1). An analysis of a set of 3D structures of proteins containing chloride anions has shown that the sidechain of arginine interacts much more frequently with chlorides than that of lysine (Carugo, 2014), suggesting that these interactions may be better described by the MARTINI force field.

Furthermore, our CG MD simulations also showed that, at low ionic concentration, VDAC lumen is more selective to anions when embedded in a POPE membrane compared to a POPC one as experimentally observed in plant VDAC (Mlayeh et al., 2017). Our results point to several acidic residues located at the rims of the β-barrel which form specific persistent ionic interactions with POPE and significant less with POPC although both POPE and POPC polar head amino group bear a single positive charge. A higher anionic preference in POPE versus POPC is also found in atomistic MD simulations. Furthermore, CG simulations of VDAC performed in an equal mixture of POPE/POPC reveal an enrichment of POPE head groups over POPC ones at the surface of VDAC suggesting possible specific binding sites for POPE headgroups. This enrichment indeed promotes the formation of specific interactions with acidic residues at the edges of the pore as observed in trajectories performed in pure POPE membrane. Such mixture atomistic

simulations were not performed as they are much more computer time consuming.

In conclusion, our results suggest that CG simulations are able to reproduce, in a semi-quantitative way, features of salt and lipid-dependent VDAC selectivity in agreement with experimental data. The simulations reveal that interactions of the inorganic ions with a few basic residues give rise to the anionic preference of the VDAC pore. The molecular mechanism of lipid-dependent selectivity is related to the lipid head group that modulates the anionic selectivity of the channel by re-orientation of side chain residues from the pore. Our work is an important step toward unraveling the detailed mechanism of metabolite transport in VDAC.

Conflict of interest

None declared.

Acknowledgements

MP and EMK are Maître de recherche and Chargé de recherche, respectively, at the Fonds de la Recherche Scientifique (F.R.S.-FNRS) (Belgium). Computational resources were provided by the Consortium des Équipements de Calcul Intensif (CÉCI) and the F.R.S.-FNRS under convention 2.5020.11, together with the supercomputing facilities of the Université catholique de Louvain (CISM/UCL), the Université de Liège (ULg), ULB, and the Tier-1 supercomputer of the Fédération Wallonie-Bruxelles under grant agreement n°1117545.

Appendix A. Supplementary data

Supplementary data associated with this article can be found, in the online version, at https://doi.org/10.1016/j.chemphyslip.2018.11.002.

References

Aksimentiev, A., Schulten, K., 2005. Imaging alpha-hemolysin with molecular dynamics: ionic conductance, osmotic permeability, and the electrostatic potential map. Biophys. J. 88, 3745–3761. https://doi.org/10.1529/biophysj.104.058727.

Arnarez, C., Mazat, J.P., Elezgaray, J., Marrink, S.J., Periole, X., 2013. Evidence for cardiolipin binding sites on the membrane-exposed surface of the cytochrome bc1. J. Am. Chem. Soc. 135, 3112–3120. https://doi.org/10.1021/ja310577u.

Baaden, M., Marrink, S.J., 2013. Coarse-grain modelling of protein–protein interactions. Curr. Opin. Struct. Biol. 23, 878–886. https://doi.org/10.1016/j.sbi.2013.09.004.

Bayrhuber, M., Meins, T., Habeck, M., Becker, S., Giller, K., Villinger, S., Vonrhein, C., Griesinger, C., Zweckstetter, M., Zeth, K., 2008. Structure of the human voltage-dependent anion channel. Proc. Natl. Acad. Sci. U. S. A. 105, 15370–15375.

Best, R.B., Zhu, X., Shim, J., Lopes, P.E.M., Mittal, J., Feig, M., MacKerell, A.D., 2012. Optimization of the additive CHARMM all-atom protein force field targeting improved sampling of the backbone ϕ, ψ and side-chain χ 1 and χ 2 dihedral angles. J. Chem. Theory Comput. 8, 3257–3273. https://doi.org/10.1021/ct300400x.

Blachly-Dyson, E., Peng, S., Colombini, M., Forte, M., 1990. Selectivity changes in site-directed mutants of the VDAC ion channel: structural implications. Science 247, 1233–1236.

Bradley, R., Radhakrishnan, R., 2013. Coarse-grained models for protein-cell membrane interactions. Polymers (Basel) 5, 890–936. https://doi.org/10.3390/polym5030890.

Bussi, G., Donadio, D., Parrinello, M., 2007. Canonical sampling through velocity rescaling. J. Chem. Phys. 126, 014101. https://doi.org/10.1063/1.2408420.

Camara, A.K.S., Zhou, Y., Wen, P.-C., Tajkhorshid, E., Kwok, W.-M., 2017. Mitochondrial VDAC1: a key gatekeeper as potential therapeutic target. Front. Physiol. 8, 460. https://doi.org/10.3389/fphys.2017.00460.

Carugo, O., 2014. Buried chloride stereochemistry in the protein data bank. BMC Struct. Biol. 14, 19. https://doi.org/10.1186/s12900-014-0019-8.

Choudhary, O.P., Paz, A., Adelman, J.L., Colletier, J.-P., Abramson, J., Grabe, M., 2014. Structure-guided simulations illuminate the mechanism of ATP transport through VDAC1. Nat. Struct. Mol. Biol. 21, 626–632. https://doi.org/10.1038/nsmb.2841.

Choudhary, O.P., Ujwal, R., Kowallis, W., Coalson, R., Abramson, J., Grabe, M., 2010. The electrostatics of VDAC: implications for selectivity and gating. J. Mol. Biol. 396, 580–592. https://doi.org/10.1016/j.jmb.2009.12.006.

Colombini, M., 2016. The VDAC channel: molecular basis for selectivity. Biochim. Biophys. Acta 1863, 2498–2502. https://doi.org/10.1016/j.bbamcr.2016.01.019.

Colombini, M., 2009. The published 3D structure of the VDAC channel: native or not? Trends Biochem. Sci. 34, 382–389. https://doi.org/10.1016/j.tibs.2009.05.001.

Colombini, M., 2004. VDAC: the channel at the interface between mitochondria and the cytosol. Mol. Cell. Biochem. 256, 107–115. https://doi.org/10.1023/B:MCBI.0000009862.17396.8d.

Colombini, M., 1989. Voltage gating in the mitochondrial channel. VDAC. J. Membr. Biol. 111, 103–111. https://doi.org/10.1007/BF01871775.

De Pinto, V., Al Jamal, J.A., Palmieri, F., 1993. Location of the dicyclohexylcarbodiimide-reactive glutamate residue in the Bovine Heart Mitochondrial Porin. J. Biol. Chem. 268, 12977–12982.

Dreyer, J., Strodel, P., Ippoliti, E., Finnerty, J., Eisenberg, B., Carloni, P., 2013. Ion permeation in the NanC porin from Escherichia coli: free energy calculations along pathways identified by coarse-grain simulations. J. Phys. Chem. B 117, 13534–13542. https://doi.org/10.1021/jp4081838.

Hess, B., Bekker, H., Berendsen, H.J.C., Fraaije, J.G.E.M., 1997. LINCS: a linear constraint solver for molecular simulations. J. Comput. Chem. 18, 1463–1472. https://doi.org/10.1002/(SICI)1096-987X(199709)18:12<1463::AID-JCC4>3.0.CO;2-H.

Hiller, S., Abramson, J., Mannella, C., Wagner, G., Zeth, K., 2010. The 3D structures of VDAC represent a native conformation. Trends Biochem. Sci. 35, 514–521. https://doi.org/10.1016/j.tibs.2010.03.005.

Hiller, S., Garces, R.G., Malia, T.J., Orekhov, V.Y., Colombini, M., Wagner, G., 2008. Solution structure of the integral human membrane protein VDAC-1 in detergent micelles. Science 321 (80-), 1206–1210. https://doi.org/10.1126/science.1161302.

Hinsch, K.-D., De Pinto, V., Aires, V.A., Schneider, X., Messina, A., Hinsch, E., 2004. Voltage-dependent anion-selective channels VDAC2 and VDAC3 are abundant proteins in bovine outer dense fibers, a cytoskeletal component of the sperm flagellum. J. Biol. Chem. 279, 15281–15288. https://doi.org/10.1074/jbc.M313433200.

Hodge, T., Colombini, M., 1997. Regulation of metabolite flux through voltage-gating of VDAC channels. J. Membr. Biol. 157, 271–279. https://doi.org/10.1007/s002329900235.

Homblé, F., Krammer, E.-M., Prévost, M., 2012. Plant VDAC: facts and speculations. Biochim. Biophys. Acta 1818, 1486–1501. https://doi.org/10.1016/j.bbamem.2011.11.028.

Hosaka, T., Okazaki, M., Kimura-Someya, T., Ishizuka-Katsura, Y., Ito, K., Yokoyama, S., Dodo, K., Sodeoka, M., Shirouzu, M., 2017. Crystal structural characterization reveals novel oligomeric interactions of human voltage-dependent anion channel 1. Protein Sci. 26, 1749–1758. https://doi.org/10.1002/pro.3211.

Hung, A., Yarovsky, I., 2011. Inhibition of peptide aggregation by lipids: insights from coarse-grained molecular simulations. J. Mol. Graph. Model. 29, 597–607. https://doi.org/10.1016/j.jmgm.2010.11.001.

Im, W., Seefeld, S., Roux, B., 2000. A Grand Canonical Monte Carlo-Brownian dynamics algorithm for simulating ion channels. Biophys. J. 79, 788–801. https://doi.org/10.1016/S0006-3495(00)76336-3.

Ingólfsson, H.I., Lopez, C.A., Uusitalo, J.J., de Jong, D.H., Gopal, S.M., Periole, X., Marrink, S.J., 2014. The power of coarse graining in biomolecular simulations. Wiley Interdiscip. Rev. Comput. Mol. Sci. 4, 225–248. https://doi.org/10.1002/wcms.1169.

Jaremko, M., Jaremko, Ł., Villinger, S., Schmidt, C.D., Griesinger, C., Becker, S., Zweckstetter, M., 2016. High-resolution NMR determination of the dynamic structure of membrane proteins. Angew. Chemie - Int. Ed. 55, 10518–10521. https://doi.org/10.1002/anie.201602639.

Jo, S., Kim, T., Iyer, V.G., Im, W., 2008. CHARMM-GUI: a web-based graphical user interface for CHARMM. J. Comput. Chem. 29, 1859–1865. https://doi.org/10.1002/jcc.20945.

Kmiecik, S., Gront, D., Kolinski, M., Wieteska, L., Dawid, A.E., Kolinski, A., 2016. Coarse-grained protein models and their applications. Chem. Rev. 116, 7898–7936. https://doi.org/10.1021/acs.chemrev.6b00163.

Krammer, E.-M., Homblé, F., Prévost, M., 2013. Molecular origin of VDAC selectivity towards inorganic ions: a combined molecular and Brownian dynamics study. Biochim. Biophys. Acta 1828, 1284–1292. https://doi.org/10.1016/j.bbamem.2012.12.018.

Krammer, E.-M., Homblé, F., Prévost, M., 2011. Concentration dependent ion selectivity in VDAC: a molecular dynamics simulation study. PLoS One 6, e27994. https://doi.org/10.1371/journal.pone.0027994.

Krammer, E.-M., Saidani, H., Prévost, M., Homblé, F., 2014. Origin of ion selectivity in Phaseolus coccineus mitochondrial VDAC. Mitochondrion 19, 206–213. https://doi.org/10.1016/j.mito.2014.04.003.

Krammer, E.-M., Vu, G.T., Homblé, F., Prévost, M., 2015. Dual mechanism of ion permeation through VDAC revealed with inorganic phosphate ions and phosphate metabolites. PLoS One 10, e0121746. https://doi.org/10.1371/journal.pone.0121746.

Lee Il, K., Jo, S., Rui, H., Egwolf, B., Roux, B., Pastor, R.W., Im, W., 2012. Web interface for Brownian dynamics simulation of ion transport and its applications to beta-barrel pores. J. Comput. Chem. 33, 331–339. https://doi.org/10.1002/jcc.21952.

Lee Il, K., Jo, S., Rui, H., Im, W., 2011. Web-based interface for brownian dynamics simulation of ion channels and its application to vdac. Biophys. J. 100, 156a. https://doi.org/10.1016/j.bpj.2010.12.1068.

Lee, S., Tran, A., Allsopp, M., Lim, J.B., Hénin, J., Klauda, J.B., 2014. CHARMM36 united atom chain model for lipids and surfactants. J. Phys. Chem. B 118, 547–556. https://doi.org/10.1021/jp410344g.

Luo, Y., Egwolf, B., Walters, D.E., Roux, B., 2010. Ion Selectivity of α-Hemolysin with a β-Cyclodextrin Adapter. I. Single Ion Potential of Mean Force and Diffusion Coefficient. J. Phys. Chem. B 114, 952–958. https://doi.org/10.1021/jp906790f.

MacKerell, A.D., Bashford, D., Bellott, M., Dunbrack, R.L., Evanseck, J.D., Field, M.J., Fischer, S., Gao, J., Guo, H., Ha, S., Joseph-McCarthy, D., Kuchnir, L., Kuczera, K., Lau, F.T., Mattos, C., Michnick, S., Ngo, T., Nguyen, D.T., Prodhom, B., Reiher, W.E., Roux, B., Schlenkrich, M., Smith, J.C., Stote, R., Straub, J., Watanabe, M., Wiórkiewicz-Kuczera, J., Yin, D., Karplus, M., 1998. All-atom empirical potential for molecular modeling and dynamics studies of proteins. J. Phys. Chem. B 102, 3586–3616. https://doi.org/10.1021/jp973084f.

Marrink, S.-J., Berendsen, H.J.C., 1994. Simulation of water transport through a lipid membrane. J. Phys. Chem. 98, 4155–4168. https://doi.org/10.1021/j100066a040.

Marrink, S.J., Risselada, H.J., Yefimov, S., Tieleman, D.P., de Vries, A.H., 2007. The

MARTINI Force Field: Coarse Grained Model for Biomolecular Simulations. J. Phys. Chem. B 111, 7812–7824. https://doi.org/10.1021/jp071097f.
Mlayeh, L., Chatkaew, S., Léonetti, M., Homblé, F., 2010. Modulation of plant mitochondrial VDAC by phytosterols. Biophys. J. 99, 2097–2106. https://doi.org/10.1016/j.bpj.2010.07.067.
Mlayeh, L., Krammer, E.-M., Léonetti, M., Prévost, M., Homblé, F., 2017. The mitochondrial VDAC of bean seeds recruits phosphatidylethanolamine lipids for its proper functioning. Biochim. Biophys. Acta - Bioenergy 1858, 786–794. https://doi.org/10.1016/j.bbabio.2017.06.005.
Monticelli, L., Kandasamy, S.K., Periole, X., Larson, R.G., Tieleman, D.P., Marrink, S.-J., 2008. The MARTINI coarse-grained force field: extension to proteins. J. Chem. Theory Comput. 4, 819–834. https://doi.org/10.1021/ct700324x.
Morriss-Andrews, A., Shea, J.-E., 2014. Simulations of protein aggregation: insights from atomistic and coarse-grained models. J. Phys. Chem. Lett. 5, 1899–1908. https://doi.org/10.1021/jz5006847.
Noskov, S.Y., Rostovtseva, T.K., Bezrukov, S.M., 2013. ATP transport through VDAC and the VDAC-tubulin complex probed by equilibrium and nonequilibrium MD simulations. Biochemistry 52, 1–3. https://doi.org/10.1021/bi4011495.
Paine, P.L., Scherr, P., 1975. Drag coefficients for the movement of rigid spheres through liquid-filled cylindrical pores. Biophys. J.
Parrinello, M., Rahman, A., 1981. Polymorphic transitions in single crystals: a new molecular dynamics method. J. Appl. Phys. 52, 7182–7190. https://doi.org/10.1063/1.328693.
Peng, S., Blachly-Dyson, E., Forte, M., Colombini, M., 1992. Large scale rearrangement of protein domains is associated with voltage gating of the VDAC channel. Biophys. J. 62, 123–135. https://doi.org/10.1016/S0006-3495(92)81799-X.
Periole, X., Marrink, S.-J., 2013. The martini coarse-grained force field. Methods Mol. Biol. 2013 (924), 533–565. https://doi.org/10.1007/978-1-62703-017-5_20.
Phillips, J.C., Braun, R., Wang, W., Gumbart, J., Tajkhorshid, E., Villa, E., Chipot, C., Skeel, R.D., Kalé, L., Schulten, K., 2005. Scalable molecular dynamics with NAMD. J. Comput. Chem. 26, 1781–1802. https://doi.org/10.1002/jcc.20289.
Rostovtseva, T., Colombini, M., 1997. VDAC channels mediate and gate the flow of ATP: implications for the regulation of mitochondrial function. Biophys. J. 72, 1954–1962. https://doi.org/10.1016/S0006-3495(97)78841-6.
Rostovtseva, T., Colombini, M., 1996. ATP flux is controlled by a voltage-gated channel from the mitochondrial outer membrane. J. Biol. Chem. 271, 28006–28008. https://doi.org/10.1074/jbc.271.45.28006.
Rui, H., Lee Il, K., Pastor, R.W., Im, W., 2011. Molecular dynamics studies of ion permeation in VDAC. Biophys. J. 100, 602–610. https://doi.org/10.1016/j.bpj.2010.12.3711.
Schredelseker, J., Paz, A., López, C.J., Altenbach, C., Leung, C.S., Drexler, M.K., Chen, J.-N., Hubbell, W.L., Abramson, J., 2014. High-resolution structure and double electron-Electron resonance of the zebrafish voltage dependent anion channel 2 reveal an oligomeric population. J. Biol. Chem. 289, 12566–12577. https://doi.org/10.1074/jbc.M113.497438.
Sengupta, D., Chattopadhyay, A., 2012. Identification of cholesterol binding sites in the serotonin. J. Phys. Chem. B 116, 12991–12996. https://doi.org/10.1021/jp309888u.
Stansfeld, P.J., Hopkinson, R., Ashcroft, F.M., Sansom, M.S.P., 2009. PIP 2 -Binding site in kir channels: definition by multiscale biomolecular simulations. Biochemistry 48, 10926–10933. https://doi.org/10.1021/bi9013193.
Stansfeld, P.J., Sansom, M.S.P., 2011. Molecular simulation approaches to membrane proteins. Structure. https://doi.org/10.1016/j.str.2011.10.002.
Teijido, O., Rappaport, S.M., Chamberlin, A., Noskov, S.Y., Aguilella, V.M., Rostovtseva, T.K., Bezrukov, S.M., 2014. Acidification asymmetrically affects voltage-dependent anion channel implicating the involvement of salt bridges. J. Biol. Chem. 289, 23670–23682. https://doi.org/10.1074/jbc.M114.576314.
Ujwal, R., Cascio, D., Colletier, J.-P., Faham, S., Zhang, J., Toro, L., Ping, P., Abramson, J., 2008. The crystal structure of mouse VDAC1 at 2.3 A resolution reveals mechanistic insights into metabolite gating. Proc. Natl. Acad. Sci. 105, 17742–17747. https://doi.org/10.1073/pnas.0809634105.
Van Der Spoel, D., Lindahl, E., Hess, B., Groenhof, G., Mark, A.E., Berendsen, H.J.C., 2005. GROMACS: fast, flexible, and free. J. Comput. Chem. 26, 1701–1718. https://doi.org/10.1002/jcc.20291.
Villinger, S., Briones, R., Giller, K., Zachariae, U., Lange, A., de Groot, B.L., Griesinger, C., Becker, S., Zweckstetter, M., 2010. Functional dynamics in the voltage-dependent anion channel. Proc. Natl. Acad. Sci. 107, 22546–22551. https://doi.org/10.1073/pnas.1012310108.
Villinger, S., Giller, K., Bayrhuber, M., Lange, A., Griesinger, C., Becker, S., Zweckstetter, M., 2014. Nucleotide interactions of the human voltage-dependent anion channel. J. Biol. Chem. 289, 13397–13406. https://doi.org/10.1074/jbc.M113.524173.
Vorobyov, I., Kim, I., Chu, Z.T., Warshel, A., 2016. Refining the treatment of membrane proteins by coarse-grained models. Proteins Struct. Funct. Bioinf. 84, 92–117. https://doi.org/10.1002/prot.24958.
Wang, L., 2012. Measurements and implications of the membrane dipole potential. Annu. Rev. Biochem. 81, 615–635. https://doi.org/10.1146/annurev-biochem-070110-123033.
Wang, Y., Cohen, J., Boron, W.F., Schulten, K., Tajkhorshid, E., 2007. Exploring gas permeability of cellular membranes and membrane channels with molecular dynamics. J. Struct. Biol. 157, 534–544. https://doi.org/10.1016/j.jsb.2006.11.008.
Weiser, B.P., Salari, R., Eckenhoff, R.G., Brannigan, G., 2014. Computational investigation of cholesterol binding sites on mitochondrial VDAC. J. Phys. Chem. B 118, 9852–9860. https://doi.org/10.1021/jp504516a.
Yefimov, S., Van Der Giessen, E., Onck, P.R., Marrink, S.J., 2008. Mechanosensitive membrane channels in action. Biophys. J. 94, 2994–3002. https://doi.org/10.1529/biophysj.107.119966.
Yesylevskyy, S.O., Schäfer, L.V., Sengupta, D., Marrink, S.J., 2010. Polarizable water model for the coarse-grained MARTINI force field. PLoS Comput. Biol. 6, e1000810. https://doi.org/10.1371/journal.pcbi.1000810.
Yin, F., Kindt, J.T., 2012. Hydrophobic mismatch and lipid sorting near OmpA in mixed bilayers: atomistic and coarse-grained simulations. Biophys. J. 102, 2279–2287. https://doi.org/10.1016/j.bpj.2012.04.005.
Zachariae, U., Schneider, R., Briones, R., Gattin, Z., Demers, J., Giller, K., Maier, E., Zweckstetter, M., Griesinger, C., Becker, S., Benz, R., de Groot, B.L., Lange, A., 2012. B-barrel mobility underlies closure of the voltage-dependent anion channel. Structure 20, 1540–1549. https://doi.org/10.1016/j.str.2012.06.015.
Zambrowicz, E.B., Colombini, M., 1993. Zero-current potentials in a large membrane channel: a simple theory accounts for complex behavior. Biophys. J. 65, 1093–1100. https://doi.org/10.1016/S0006-3495(93)81148-2.